



Split ring resonator as a nanoscale optical transducer for heat-assisted magnetic recording

ANURUP DATTA, ZHOU ZENG, AND XIANFAN XU*

School of Mechanical Engineering and Birck Nanotechnology Center, Purdue University, West Lafayette, IN 47906, USA

**xxu@ecn.purdue.edu*

Abstract: Split ring resonators (SRR) are optical nanostructures that have received a lot of attention for their ability to support magnetic resonance and for their potential use as materials with negative dielectric constant. In this work, we design SRRs as near-field transducers (NFT) for generating a nanoscale hotspot in heat-assisted magnetic recording (HAMR), which is considered a candidate for the next-generation data storage technology. The underlying mechanisms for the generation of hotspot and the dependence on wavelength and geometry of the SRR structure are studied. Optical and thermal performance of SRRs functioning as NFTs in a HAMR device are evaluated. These structures were fabricated using focused ion beam milling. The focusing capability of the SRR is experimentally demonstrated using a scattering near field scanning optical microscope.

© 2019 Optical Society of America under the terms of the [OSA Open Access Publishing Agreement](#)

1. Introduction

Generation of a focused optical spot beyond the diffraction limit has received a whole lot of attention due to its wide potential applications in the field of nanophotonics [1,2]. Heat assisted magnetic recording (HAMR) is one such area of commercial importance where nanoscale hotspot plays a significant role in developing the next generation hard disk drives [3–6]. Contemporary hard disk drives based on perpendicular magnetic recording technology and shingled magnetic recording have reached the practical limits of data storage density due to the physical constraint imposed by the superparamagnetic limit of the recording medium [7]. Further novelties in the recording medium technology to achieve higher density data storage necessitates the use of a medium with higher coercivity, which helps in stabilizing the orientations of the magnetic bits at room temperature. But in order to write data into the high coercivity medium, its temperature needs to be raised temporarily to lower the medium coercivity [8]. HAMR technology promises to address this challenge by locally heating the recording medium over a tiny area of tens of nanometers through the use of a plasmonic antenna, also known as near field transducer (NFT). This localized heating of the recording medium allows the magnetic writing to occur only at the high temperature region. Hence, the NFT design needs to be able to generate a tiny hotspot for the proper functioning of a HAMR device.

Producing a sub diffraction limited hotspot generally requires appropriately designed subwavelength structures which can be optically excited by properly polarized incident light. Several different types of antenna-based and aperture based designs have been proposed as NFTs and their optical and thermal performance have been studied for their usage in a HAMR device [5,9,10]. NFT designs are geometrically optimized to support localized surface plasmon resonance at a specific operating wavelength which helps in enhancing the intensity of the near field spot. Typically, an NFT design contains some sharp features such as notches and ridges which help in concentrating the electric field through the lightning rod effect for producing a very tiny spot size in the near field [11–14]. Also, tiny gaps in a metallic

structure like a cross sectional ridge aperture can be exploited for subwavelength confinement of the incident light [15].

In this work, we explore the use of a nanoscale split-ring resonator (SRR) for the purpose of generating a nanoscale hot spot. SRRs have been studied extensively for their unique capability of generating magnetic resonance and can be used for creating materials with negative dielectric constant [16–19]. SRRs have the advantage that they have a very small size at the resonance condition [20] and the electric field can be concentrated well within a tiny gap resulting in a very small optical spot. It is also compatible for the placement of a magnetic write pole in the vicinity of the NFT in a HAMR device. Functionally, the near field performance of an SRR structure resembles the widely studied C apertures and ridge waveguides [12,21–24]. Like these structures, the resonant transmission and focusing in an SRR is influenced by the dimensions of the structures and its ability to support a TE like mode. In the next section, the SRR structure is described first and the underlying mechanisms for the generation of a hotspot at different wavelengths are explained. Wavelength dependent study incorporating the geometric variation of the structure is explored in the presence of a recording medium through electromagnetic simulations. Subsequent thermal simulations were also performed to predict the temperature rise and thermal figure of merit for HAMR devices. For feasibility studies, such structures were fabricated using focused ion beam milling. It should be noted that for bulk production, other fabrication methods such as planar lithographic fabrication techniques combined with thin film deposition can be used. Optical characterization of the near field spot is performed using a scattering near field scanning optical microscope (s-NSOM). A localized hotspot is demonstrated which prove the focusing capability of the SRR beyond the diffraction limit.

2. Description of the SRR structure

SRRs are antenna-based optical nanostructures which can either have a single loop or a double loop. The single loop SRR consists of a metallic ring like structure with a small gap between the ends of the ring as shown in Fig. 1(a). The optical resonance of the SRR can be either of a plasmonic origin or an LC-circuit origin. The LC circuit resonance can be understood by drawing an analogy to the resonance condition of an electrical circuit involving capacitance and inductance. In the case of an SRR, the small gap acts as the capacitive portion of the resonant circuit with a capacitance C while the metallic ring constitutes the inductive portion of the circuit with an inductance L [16,20,25]. The equivalent LC circuit representation is shown in Fig. 1(b).

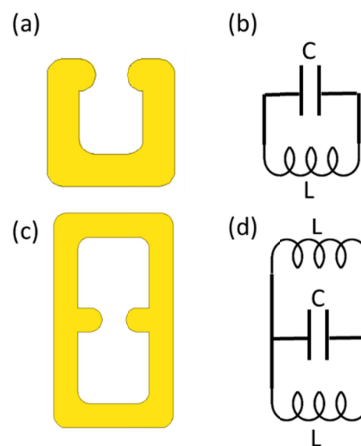


Fig. 1. (a) Schematic of a single loop split ring resonator nanostructure, (b) its equivalent LC circuit, (c) double loop SRR and (d) its equivalent LC circuit.

On the other hand, a double loop SRR consists of two ring like structures with a single gap between the two arms as shown in Fig. 1(c) while the equivalent LC circuit representation shown in Fig. 1(d) has two inductive loops and a single capacitor. The resonance frequency of SRR LC-circuit is inversely proportional to the square root of the inductance and the capacitance of the structure. The LC-circuit resonance is defined by a single oscillating current along the loops of the SRR. Near the resonance, there is a strong electric field across the capacitive gap of the SRR structure which gives rise to a strong field enhancement. When combined with the effect of the small gap between the two arms of the SRR, an enhanced and focused hot spot is formed in the gap of the SRR.

Apart from the LC-circuit resonance, other plasmon resonances are also observed at different wavelengths depending on the dimensions of the SRR geometry [26–29]. These plasmon resonances are similar to the resonances which are found in other plasmonic structures. The SRR design allows both LC type of resonance as well as plasmonic resonances to be used for generating a localized hotspot.

Initial experiments on the SRR structures demonstrated their capability to support magnetic resonances and negative permeability in the GHz range following the work of Pendry et al. [17], and subsequently resonances have been demonstrated in the 100 THz regime and even in the visible spectral range [16,30,31]. Figures 2(a)–(c) show the possible propagating directions of the incident light and the orientation of the magnetic field and the electric field vectors for exciting the resonance modes in the SRR structure [19]. One of the primary ways for the excitation of the LC resonance mode is ensuring that the magnetic field vector \mathbf{H} , is perpendicular to the plane of the SRR loop as shown in Figs. 2(a) and (b). This requires that the propagating direction of the incident light is along the plane of the structure. An alternate way to excite the LC resonance mode is if the electric field vector \mathbf{E} , of the incident light is pointed across the gap between the two arms of the SRR as shown in Fig. 2(c), which introduces an oscillating current around the SRR loop [16,32]. This electric excitation of the SRR cannot only couple to the LC circuit resonance mode but also to other plasmonic modes depending on the geometric dimensions of the SRR, which will be discussed in detail in the next section.

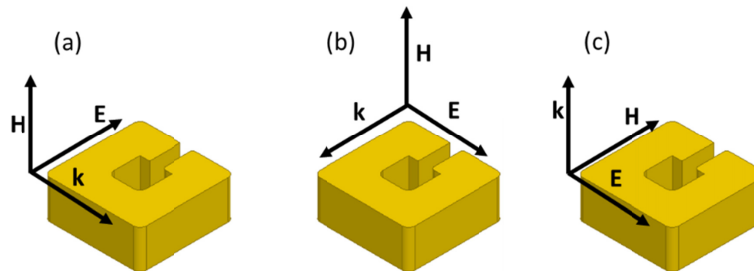


Fig. 2. Possible orientations of the propagation vector of the incident light and the electric and magnetic field polarizations to excite resonance mode in the SRR structure. (a) The magnetic field is pointed out-of the plane with the electric field pointed parallel to the gap, (b) The magnetic field is pointed out of the plane with the electric field pointed across the gap and (c) The propagation vector is pointed out of the plane with the electric field pointed across the gap.

3. Design of an SRR for HAMR

The potential of using an SRR as an NFT for a HAMR system is explored in this section. We consider both a single loop SRR and a double loop SRR, noting that a single loop SRR would be more suitable for HAMR due to the need of placing a magnetic pole near the hot spot. The E field can be pointed across the arms of SRR and hence the resonance modes are excited by the electric excitation as shown in Fig. 2(c). This kind of excitation scheme for a HAMR system has been demonstrated by Stipe et al. [13] for another type of NFT and has been

chosen in this study due to its compatibility with the focused ion beam fabrication process. The SRR geometry also supports other excitation schemes such as in Figs. 2(a) or (b) wherein the NFT could be located in a plane perpendicular to the recording medium and could be fabricated through planar fabrication techniques [14]. For an SRR structure, all the dimensions such as the gap width, g , the horizontal base length, l_x , the vertical arm length, l_y and the width of the arms, w , are important for supporting different resonant modes at different wavelengths [27]. Figure 3 shows the relevant parameters of a single loop SRR as well as the relative position of the magnetic pole and the recording medium. Full wave 3D electromagnetic (EM) simulations were performed using ANSYS HFSS. We assume a 600 nm diameter Gaussian beam (which should be achievable using high performing focusing optics even at longer wavelengths around ~ 1700 nm) incident on the NFT. The simulation model consists of different layers within the recording medium and their thickness and properties are elaborated in Table 1 [10,33]. The dimension in the X-Y plane was considered to be $3\mu\text{m} \times 3\mu\text{m}$ with only half the space along Y direction being simulated by making use of the symmetry condition. Adaptive mesh sizing was used throughout the model to discretely mesh the computational area and additionally extra meshing controls such as body sizing and edge sizing were used to coerce a sufficiently high mesh density in the critical regions such as NFT and the recording medium.

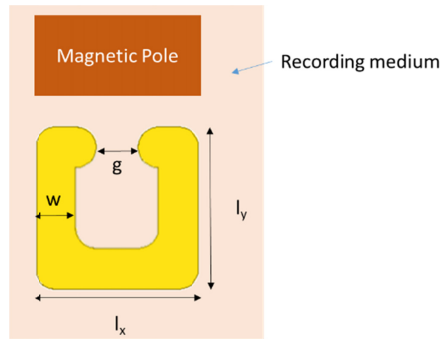


Fig. 3. Schematic of a single loop SRR showing the relevant parameters and the placement of the magnetic pole and the recording medium.

The SRR was considered to be made of gold and the recording medium was considered to be made of FePt. The optical figure of merit was taken as the coupling efficiency into the recording medium and was calculated as the ratio of the power absorbed in the recording medium in a disk of diameter 70 nm to the incident power. In the context of a HAMR system, the spot size is largely dependent on the gap between the two arms of the SRR ring and the different resonant modes in the SRR NFT give rise to different coupling efficiencies at different wavelengths. Coupled thermal simulation were done following the EM simulations using ANSYS Workbench. The absorbed power in the recording medium and the NFT were

calculated as $q''' = \frac{1}{2} \epsilon_0 \omega \text{Im}(\epsilon) |E|^2$, where ϵ is the relative permittivity, ϵ_0 is the vacuum permittivity, and ω is the angular frequency. q''' is taken as the heat generation term while solving the heat diffusion equation to calculate the temperature profile of the NFT and the recording medium. Constant temperature boundary conditions were assumed at the outer faces of the model. Considering the fact that an NFT is continuously heated, the NFT temperature is noted at the steady state while the temperature of the recording medium is noted at the end of 1 ns taking into account the rotation of the recording medium [36]. $\Delta T_{\text{medium}} / \Delta T_{\text{NFT}}$ is considered as the thermal figure of merit which is given by the ratio of the temperature rise of the recording medium versus the temperature rise of the NFT and a higher number is beneficial for improved reliability of the HAMR device.

Table 1. Different layers in the recording medium and their properties

Material	Optical Properties			Thermal Properties		
	Thick-ness [nm]	n	k	Vertical thermal conductivity (W/mK)	Lateral thermal conductivity (W/mK)	Density x Specific Heat ($\rho * c_p$) (J/m ³ -K) x10 ⁶
Heat sink ^a	100	0.26	5.28	150	150	3.3
Interlayer	15	1.7	0	10	10	1.9
Storage medium ^b	10	Wavelength dependent		7	1.5	3.2
Media overcoat	2.5	2.3	0	2	2	1.76
Air	2.5	1	0	0.02	0.02	0.001225
Lube	1	1	0	0.02	0.02	0.001225
Head overcoat	2.5	2.5	0	2	2	1.76
NFT – Au ^c	Variable	Wavelength dependent		314	314	2.5
Substrate (quartz)	Infinite (600 nm in model)	1.5	0	1	1	2

^aProperties of heat sink material was obtained from ASTC (Advanced Storage Technology Consortium) reference sheet.

^bWavelength dependent optical properties of storage medium obtained from [34].

^cWavelength dependent optical properties of NFT-Au obtained from [35].

3.1. Resonant modes of a single loop SRR

We consider a single loop SRR where, the gap, g is taken as 20 nm, the width of the arms of the SRR, w is 30 nm, the length of each of the arms, l_x and l_y is 90 nm, and the thickness of the gold film is taken to be 60 nm. A fillet of radius 5 nm is assumed at the sharp corners of the arms of the SRR. The dimensions of the SRR are chosen such that two resonance peaks are observed in the range between 600 nm and 1700 nm. For the dimensions described above, two resonance peaks, one near 800 nm and other near 1550 nm are observed as shown in Fig. 4. The two peaks correspond to two different resonance modes supported by the NFT. The origin of the resonance modes can be explained from the fields at different wavelengths.

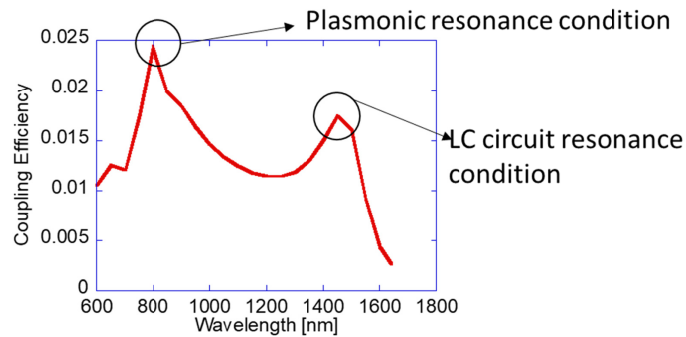


Fig. 4. Coupling efficiency versus wavelength for a single loop SRR.

Figures 5(a)–(c) show field distributions corresponding to the resonance mode at 1550 nm. From the electric field in Fig. 5(a), it is seen that there is only one single hotspot at the gap between the two arms of the SRR. Figure 5(b) shows the surface current density at the NFT surface. The white arrow in the figure shows the movement of the surface current along the top surface of the NFT and the surface current moves in a single oscillatory loop. The pattern of the surface current flow is strongly related to the magnetic field response from the structure. Figure 5(c) shows the out-of-plane H field component and it is seen that there is a strong concentration of the H field in the central gap of the SRR. Even though the incident field does not have an out-of-plane magnetic field component, the incident electric field drives an oscillating current which induces a strong magnetic field response from the SRR. Following Ampere’s circuital law, the out-of-plane magnetic response is directly related to the surface current flow around the loop of the SRR as denoted by the white arrow in Fig. 5(b). This magnetic field response is a characteristic of the LC circuit mode and hence this resonance mode can be considered as a LC circuit resonance mode. The SRR structure can support the LC mode only when the geometric dimensions allow a circular loop flow of surface current density along the perimeter of the structure and the frequency at which this

can happen is $\omega_0 = \frac{1}{\sqrt{L_{eff}C_{eff}}}$, where, L_{eff} is the effective inductance and C_{eff} is the effective

capacitance of the loop [20]. The values of L_{eff} and C_{eff} are strongly dependent on the geometric dimensions of the structures, hence changing the geometric parameters or the wavelength strongly affects the strength of the LC mode. The peak out-of-plane magnetic field in the LC mode is 750 Oe for 5 mW incident laser power while the H field that is typically used in high density perpendicular recording fields is in the vicinity of 20kOe [3]. Hence, the out-of-plane magnetic field from the NFT will not have any significant effect on the magnetic writing. On the other hand, Figs. 5(d)–(f) correspond to a plasmonic resonance condition at 800 nm where in addition to the strong hotspot at the gap of the two arms, there are also field concentrations near the two ends of the base of the SRR. This can be understood by looking at the surface current density in Fig. 5(e). In this plasmonic resonance mode, it can be seen that the surface current actually follows a complex path on the surface of the SRR. There is a portion of the current that flows across the base of the horizontal base of the SRR and creates a dipole like charge concentration which is similar to a plasmonic mode. This causes two additional hot spots at the ends of the horizontal base. Besides, the surface charge also flows along the two vertical arms of the SRR from the ends of its horizontal base and gives rise to an increased field concentration at the gap region of the SRR. These surface current flows are related to the magnetic field response from the structure. Figure 5(f) shows the out-of-plane H field component. The response of the H field from the SRR structure is quite weak at the center of the structure and hence this mode does not have a strong LC

circuit origin, but this magnetic field drives the current flows along the vertical arms. Another stronger magnetic field is near the horizontal portion of the SRR, which causes the surface current flow at the base of the SRR.

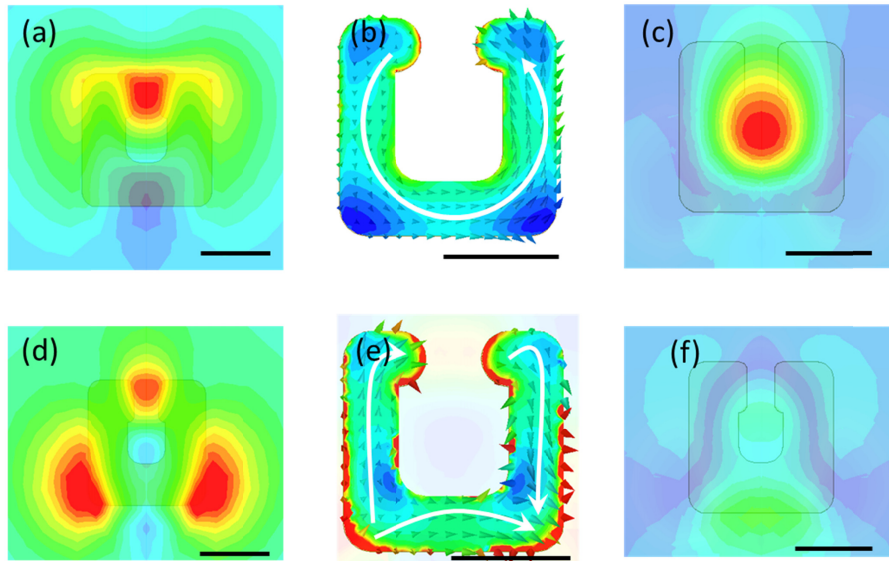


Fig. 5. (a) Electric field profile at the recording medium at 1550 nm, (b) Current density at the surface of the NFT at 1550 nm, (c) Out-of-plane magnetic field at the recording medium at 1550 nm. (d) Electric field profile at the recording medium at 800 nm, (e) Current density at the surface of the NFT at 800 nm and (f) Out-of-plane magnetic field at the recording medium at 800 nm. Scale bar in these figures is 50 nm.

Higher order plasmonic modes can be observed either by changing the dimensions of the SRR antenna or by changing the wavelength. The width, w and the arm length l_x of the SRR are varied and the variation of coupling efficiency versus the wavelength is shown in Figs. 6(a)–(d) for different values of l_x and w . The appearance of different resonance peaks and their shift with wavelength is observed. Figure 6(a) shows the coupling efficiency as a function of wavelength for various values of w for $l_x = 90$ nm and Figs. 6(b)–(d) show the coupling efficiency for $l_x = 150$ nm, 200 nm, and 250 nm respectively. The numbers in the figures at the resonance peaks denote the different excitation modes of the SRR antenna. From Fig. 6(a), it is seen that when $l_x = 90$ nm and $w = 30$ nm, two different resonance peaks, (1) and (2) corresponding to two different modes are present. Resonance peak (1) corresponds to the LC circuit mode as explained earlier and peak (2) corresponds to a plasmonic mode. When w is decreased to smaller values, the resonance peaks redshift. The likely reason for this redshift is that with the decrease in w , there is a decrease in current and hence a higher inductance and a lower resonant frequency. On the other hand, with the increase in l_x , the characteristic length of the SRR increases. It is known that for a plasmonic structure, the resonance wavelength increases with the length of the structure, hence the resonance peaks redshift with the increase in l_x [37]. In Fig. 6(b), the arm length is changed to $l_x = 150$ nm and the coupling efficiency is plotted for different values of w at different wavelengths. With the increase in l_x , it is seen that there is a substantial redshift of the resonance peak (2) which can be verified by observing the qualitative nature of the electromagnetic field plots (not shown here). Also, the resonance peak (3) corresponding to the next higher order plasmonic mode appears. A high coupling efficiency of 3.1% is obtained at 750 nm corresponding to the resonance peak (3). When l_x is increased further to 200 nm or 250 nm as shown in Figs. 6(c) and (d) respectively, the resonance peaks redshift further and peak (4) appears. As the size of the antenna gets bigger, the surface current follows a more complicated pattern and for these

higher order modes, some additional hot spots can be observed near the edges of the arms of the SRR antenna.

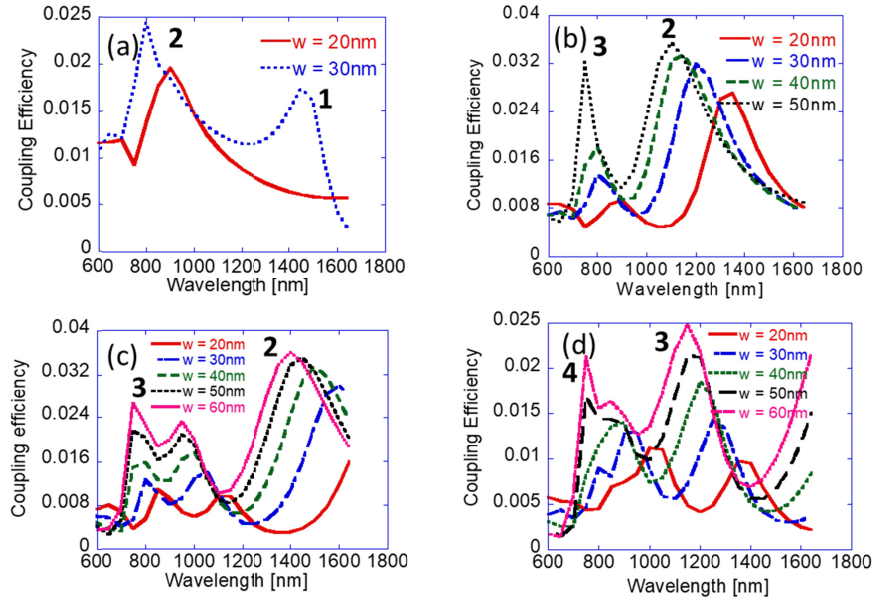


Fig. 6. Coupling efficiency into the recording medium versus wavelength for different values of w and the arm length l_x . (a) $l_x = 90$ nm, (b) $l_x = 150$ nm, (c) $l_x = 200$ nm and (d) $l_x = 250$ nm.

3.2. Resonant modes of a double loop SRR

The characteristics of the resonances of the double loop SRR are quite similar to that of the single loop SRR. The schematic of the double loop SRR is shown in Fig. 7(a). It consists of two inductive loops and a single capacitive gap between the two arms. The presence of two loops allows more surface charges to concentrate near the gaps, making the resonance peaks more intense. Figures 7(b)–(d) show coupling efficiency into the recording medium as a function of the wavelength for different widths, w and $l_x = 120$ nm, 150 nm and 250 nm respectively. In these simulations, l_y is taken to be equal to l_x . From Fig. 7(b), which shows the coupling efficiency for $l_x = 120$ nm for different values of w , the resonance peaks (1) and (2) corresponding to different modes are seen. Resonance peak (1) is the LC circuit resonance mode and the relevant field quantities are shown in Figs. 8(a)–(c).

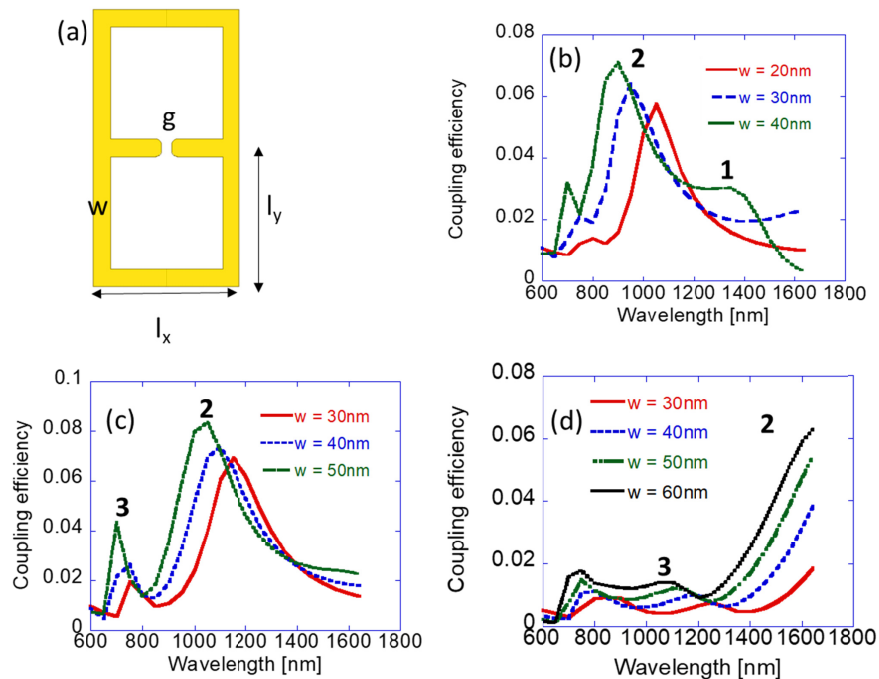


Fig. 7. (a) Schematic of the double loop SRR with the relevant dimensions, (b) Coupling efficiency into the recording medium versus wavelength for different values of w and the arm length l_x . (b) $l_x = 120$ nm, (c) $l_x = 150$ nm and (d) $l_x = 250$ nm.

Similar to the single loop SRR structure, resonance peak (1), shown in Fig. 7(b), is the LC circuit resonance mode. The electric field distribution and the surface current movement at the surface of the SRR are shown in Figs. 8(a) and (b), respectively. The surface current moves in two separate loops along the arms of the double loop SRR and then they converge near the gap generating a hot spot. Also, the strong response of the out-of-plane magnetic field from the structure is seen in Fig. 8(c). The two separate loops of the surface current are related to the two separate magnetic hotspots seen in Fig. 8(c). The maximum coupling efficiency reaches to 7% for the resonance peak (2) shown in Fig. 7(b). Due to the effect of the two loops, the maximum coupling efficiency for the double loop SRR is about twice that of the single loop SRR. The corresponding electric field distribution, the surface current movement at the surface of the SRR and the out-of-plane magnetic field plot are shown in Figs. 8(d)–(f), respectively which denotes a plasmonic mode. The response of the out-of-plane magnetic field from the structure is weak as seen from Fig. 8(f) and the multipolar nature of the magnetic hotspots gives rise to the surface current patterns as seen in Fig. 8(e). From Figs. 7(c) and (d), similar to the trend noticed in the single loop SRR, we find that with the increase in w , the resonance peaks move to a shorter wavelength regime while with the increase in l_x , the resonance peaks move towards longer wavelengths and higher order plasmonic mode, denoted by (3) begins to appear. Also similar to the single loop SRR, a decrease in w causes a redshift of the resonance wavelength.

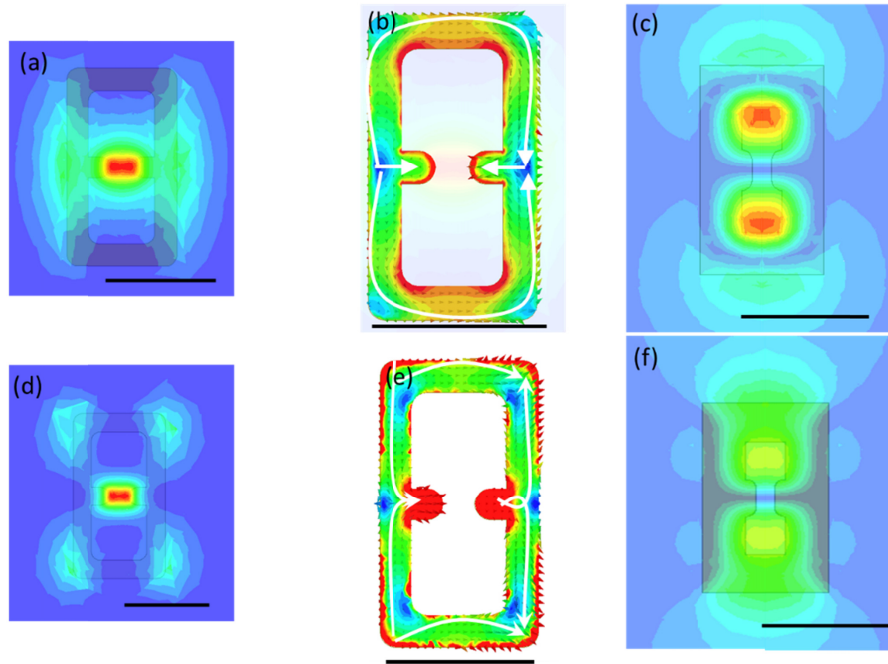


Fig. 8. (a) Electric field profile at the recording medium corresponding to mode (1), (b) Surface current density of the NFT for mode (1), (c) Out-of-plane magnetic field for mode (1), (d) Electric field profile at the recording medium corresponding to mode (2), (e) Surface current density at the surface of the NFT for mode (2) and (f) Out-of-plane magnetic field for mode (2). (Modes (1) and (2) denote the resonance peaks as seen in Fig. 7(b)). Scale bar in these figures is 150 nm.

3.3. Thermal simulations of SRR

In order to investigate the thermal performance of SRR, we study the single loop and double loop SRR designs which have been optimized to have the highest coupling efficiency in the near IR wavelength range (700 nm – 900 nm) since this is the standard wavelength for HAMR devices. It is noted here that, in this wavelength range, the SRR structures are able to support mostly plasmonic resonances as can be seen from Figs. 6 and 7. The LC type of resonances are generally present in longer wavelength regimes. If longer wavelength are used in HAMR devices there can be significant benefits from using the LC type resonances of these SRR structures including (i) LC type of resonance mode has a single hotspot at the gap unlike plasmonic resonances where apart from the hotspot at the gap of the SRR, other weak secondary hotspots are found at the edges of the structures and (ii) Utilizing the LC resonance mode in the longer wavelength regime also ensures that less absorption of the incident power in the NFT. This is due to the decreasing absorptivity of gold with increase in wavelength [29]. Thus, utilizing the LC type of resonances in the longer wavelength regime can lead to lower temperature rise of the NFT. In the remaining portion of the thermal simulations we focus on wavelengths in the 700 nm to 900 nm range due to its current commercial implications.

First, a single loop SRR design is chosen having dimensions of $l_x = 150$ nm, $w = 50$ nm which has the highest coupling efficiency of 3.1% at 750 nm for a single loop SRR based on Fig. 6(b). Coupled thermal simulations were done to calculate the temperature rise of the recording medium and the NFT. For an input power of 5 mW, the temperature of the recording medium at the end of 1 ns is shown in Fig. 9(a) while the steady state temperature of the NFT is shown in Fig. 9(b). The maximum temperature of the recording medium reaches 993 K at the end of 1 ns while that for the NFT reaches 875 K at the steady state.

Accordingly, the thermal figure of merit, $\Delta T_{\text{medium}} / \Delta T_{\text{NFT}}$ is 1.2. Next, for the case of the double looped SRR, we choose a design which has the highest coupling efficiency for a double loop SRR. Based on Fig. 7(b), a double looped SRR of dimensions: $l_x = 120$ nm, $w = 40$ nm, wavelength = 800 nm has a coupling efficiency of 7.1%. For an input power of 5 mW, the temperature of the recording medium at the end of 1 ns is shown in Fig. 9(c) while the steady state temperature of the NFT is shown in Fig. 9(d). The maximum temperature of the recording medium is 1166 K while that for the NFT, the temperature is 657 K. It must be noted that the maximum temperature rise is directly proportional to the input power and would decrease with decreasing the input power. The thermal figure of merit $\Delta T_{\text{medium}} / \Delta T_{\text{NFT}}$ is 2.40. The two loops of the SRR help in achieving a better coupling efficiency which translates to an improved thermal figure of merit. Also, greater size of the NFT for the double loop SRR helps in dissipating heat over a larger volume leading to a lower rise in the temperature of the NFT and hence, a better thermal figure of merit.

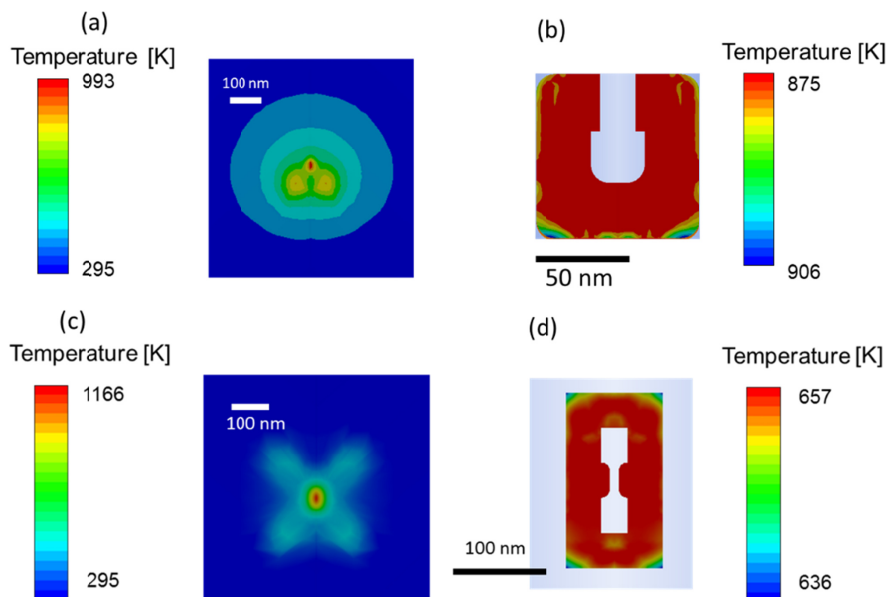


Fig. 9. For a single loop SRR, temperature plots of (a) recording medium at the end of 1 ns and (b) the NFT at steady state. For a double loop SRR, temperature plots of (c) recording medium at the end of 1 ns and (d) the NFT at steady state.

4. Fabrication and experimental characterization of SRR using s-NSOM

The near field focusing characteristics of the fabricated single looped SRR structures are studied using scattering near field scanning optical microscope (s-NSOM). Since s-NSOM experiments are performed without the nearby recording medium, the resonance conditions for the generation of an enhanced hot spot will be different from that in the presence of a recording medium. Additional simulations were done to find the dimensions of the SRR in air which has a strong enhanced field at the gap of the SRR. It was found that for the dimensions: $w_y = 50$ nm, $l_x = 220$ nm, $g = 20$ nm and thickness = 100 nm, a resonance peak is observed near 800 nm (which is the wavelength of interest for HAMR applications and matches closely with the 785 nm laser used for the s-NSOM measurements). Accordingly, SRR structures of these dimensions were fabricated. First, gold of 100 nm thickness was deposited on a glass substrate by e-beam evaporation after a deposition of 5 nm titanium for adhesion. Then focused ion beam milling (FIB) was used to mill away the portion of the gold so that we are finally left with the shape of the SRR. A minimum FIB current of 1 pA was used to ensure

fine resolution of the feature size and to produce structures with a very small size. Figures 10(a) – (c) show a series of SRR structures formed by this method.

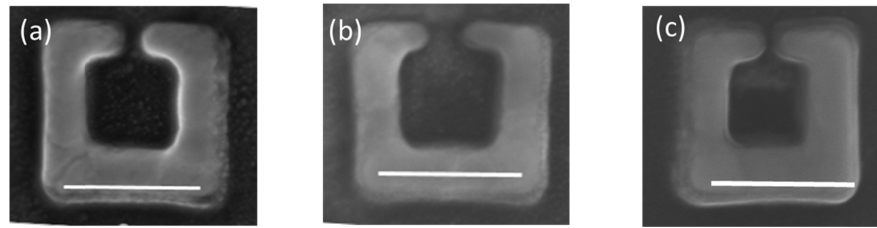


Fig. 10. (a), (b) and (c) SEM images of SRR structures fabricated through FIB milling. Scale bar is 200 nm.

The s-NSOM characterization studies of the SRR structures were carried out in the transmission mode. In an s-NSOM measurement, the structure is scanned in an AFM in the tapping mode. At the same time, the structures are optically excited by a focused laser beam (wavelength - 785 nm) with a polarization across the gap of the SRR structures. The oscillation of the tip relays the near field radiation pattern of the structures to the far field where it is collected by a photodetector. A lock-in amplifier-based detection scheme is used to demodulate the collected photo diode signal at the tip oscillating frequency and its higher harmonics. Higher harmonics such as 2nd and 3rd harmonic demodulation helps in reducing the background noise and unravelling the true near field spot [34,35,39]. The measured spot size approaches very close to that of the actual near field profile for demodulation between third and fifth order components [38]. However, considering the signal-to-noise ratio which decreases with increasing harmonic order, third harmonic demodulation is used here as representative of the near field spot. Details of the experimental setup and the related detection scheme is described elsewhere [34]. The s-NSOM results are shown in Fig. 11. Figure 11(a) shows the SEM image of the fabricated SRR structure, (b) the topography measured by AFM, and the s-NSOM images taken at 2nd and 3rd harmonic of the tip modulation frequency are shown in Figs. 11(c) and (d) respectively. The field concentration and enhancement at the gap of the SRR is clearly seen from Figs. 11(c) and (d) and the spot size as measured from the 3rd harmonic image is 30 nm x 65 nm. Due to the finite size of the AFM tip, the SRR image obtained from the AFM measurement in Fig. 11(b) has larger dimensions by about 10 nm (the nominal radius of the AFM tip apex), than what is observed from the SEM image. The actual near field spot size is also affected by AFM tip effects and when compensated for the tip dimension by using a Gaussian sharpening filter of mask size of 20 nm (based on the AFM tip diameter), the calculated spot size comes out to be 25 nm x 54 nm. The spot size from the simulation at the exit plane is 15 nm x 50 nm and hence is close to the calculated spot size after compensating for the tip effect. It is also noted that the dimensions of the fabricated structure as determined from Fig. 11(a) are $l_x = 264$ nm, $l_y = 237$ nm, $w_x = 62$ nm and $w_y = 66$ nm, and the gap size being 28 nm x 45 nm, which are slightly different from the intended dimensions of $l_x = l_y = 220$ nm and $w_x = w_y = 50$ nm and gap dimension of 20 nm x 50 nm. However, this slight deviation does not affect the near field focusing ability of the structure as seen from the s-NSOM results.

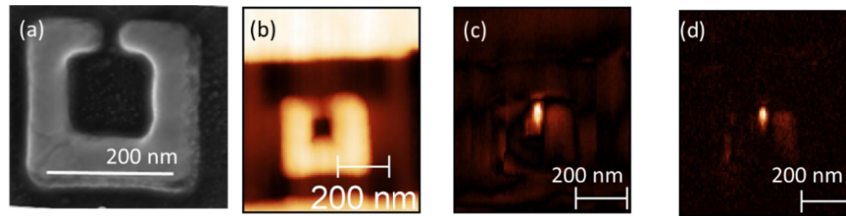


Fig. 11. s-NSOM results of SRR structure. (a) SEM image of an SRR structure, (b) AFM topography, (c) 2nd harmonic image of s-NSOM signal, and (d) 3rd harmonic image of s-NSOM signal.

5. Conclusions

In this study, SRRs are investigated as potential nanostructures for their use as NFTs in a HAMR device. The different resonant modes including the LC circuit mode and higher order modes can be used to design structures which are resonant at a particular wavelength and can serve as a guideline for designing near field transducers with high coupling efficiency. Through the study of both single loop and double loop structures, the optical and thermal functionalities of these optical nanostructures were explored and a high coupling efficiency of 7.2% was found to be achievable through the use of double loop structures. In addition, in order to characterize the near field concentration and the spot size of the SRRs, SRRs were fabricated and then characterized using s-NSOM. Optical characterization shows the presence of a focused near field spot, consistent with the numerical design. Further simulation studies would include the placement of the magnetic pole near the vicinity of the NFT and its effect on the overall performance. Overall, it can be concluded that SRRs structures can potentially serve as alternate designs of NFT structures due to their ability to achieve high coupling efficiencies and support different type of resonances at different wavelengths.

Funding

Advanced Storage Technology Consortium (ASTC); National Science Foundation (CMMI-1634832).

Acknowledgments

The authors would like to thank Prabhukumar Venuthurumilli for help with the sample fabrication.

References

1. J. A. Schuller, E. S. Barnard, W. Cai, Y. C. Jun, J. S. White, and M. L. Brongersma, "Plasmonics for extreme light concentration and manipulation," *Nat. Mater.* **9**(3), 193–204 (2010).
2. D. K. Gramotnev and S. I. Bozhevolnyi, "Plasmonics beyond the diffraction limit," *Nat. Photonics* **4**(2), 83–91 (2010).
3. R. E. Rottmayer, S. Batra, D. Buechel, W. A. Challener, J. Hohlfeld, Y. Kubota, L. Li, B. Lu, C. Mihalcea, K. Mountfield, K. Pelhos, C. Peng, T. Rausch, M. A. Seigler, D. Weller, and X.-M. Yang, "Heat-assisted magnetic recording," *IEEE Trans. Magn.* **42**(10), 2417–2421 (2006).
4. L. Pan and D. B. Bogy, "Data storage: Heat-assisted magnetic recording," *Nat. Photonics* **3**(4), 189–190 (2009).
5. N. Zhou, X. Xu, A. T. Hammack, B. C. Stipe, K. Gao, W. Scholz, and E. C. Gage, "Plasmonic near-field transducer for heat-assisted magnetic recording," *Nanophotonics* **3**(3), 141–155 (2014).
6. M. A. Seigler, W. A. Challener, E. Gage, N. Gokemeijer, G. Ju, B. Lu, K. Pelhos, C. Peng, R. E. Rottmayer, X. Yang, H. Zhou, and T. Rausch, "Integrated heat assisted magnetic recording head: Design and recording demonstration," *IEEE Trans. Magn.* **44**(1), 119–124 (2008).
7. M. P. Sharrock, "Time-dependent magnetic phenomena and particle-size effects in recording media," *IEEE Trans. Magn.* **26**(1), 193–197 (1990).
8. M. H. Kryder, E. C. Gage, T. W. McDaniel, W. A. Challener, R. E. Rottmayer, G. Ju, Y.-T. Hsia, and M. F. Erden, "Heat assisted magnetic recording," *Proc. IEEE* **96**(11), 1810–1835 (2008).
9. W. A. Challener and A. V. Itagi, "Near-Field Optics for Heat-Assisted Magnetic Recording (Experiment, Theory, and Modeling)," in *Modern Aspects of Electrochemistry No. 44: Modelling and Numerical Simulations II*, M. Schlesinger, ed. (Springer, 2009), pp. 53–111.

10. A. Datta and X. Xu, "Comparative study of optical near-field transducers for heat-assisted magnetic recording," *Opt. Eng.* **56**(12), 121906 (2017).
11. N. Zhou, L. M. Traverso, and X. Xu, "Power delivery and self-heating in nanoscale near field transducer for heat-assisted magnetic recording," *Nanotechnology* **26**(13), 134001 (2015).
12. E. X. Jin and X. Xu, "Finite-difference time-domain studies on optical transmission through planar nano-apertures in a metal film," *Jpn. J. Appl. Phys.* **43**(1), 407–417 (2004).
13. B. C. Stipe, T. C. Strand, C. C. Poon, H. Balamane, T. D. Boone, J. A. Katine, J.-L. Li, V. Rawat, H. Nemoto, A. Hirotsune, O. Hellwig, R. Ruiz, E. Dobisz, D. S. Kercher, N. Robertson, T. R. Albrecht, and B. D. Terris, "Magnetic recording at 1.5 Pb m^{-2} using an integrated plasmonic antenna," *Nat. Photonics* **4**(7), 484–488 (2010).
14. W. A. Challener, C. Peng, A. V. Itagi, D. Karns, W. Peng, Y. Peng, X. Yang, X. Zhu, N. J. Gokemeijer, Y.-T. Hsia, G. Ju, R. E. Rottmayer, M. A. Seigler, and E. C. Gage, "Heat-assisted magnetic recording by a near-field transducer with efficient optical energy transfer," *Nat. Photonics* **3**(4), 220–224 (2009).
15. L. Traverso, A. Datta, and X. Xu, "Subdiffraction light focusing using a cross sectional ridge waveguide nanoscale aperture," *Opt. Express* **24**(23), 26016–26023 (2016).
16. S. Linden, C. Enkrich, M. Wegener, J. Zhou, T. Koschny, and C. M. Soukoulis, "Magnetic response of metamaterials at 100 terahertz," *Science* **306**(5700), 1351–1353 (2004).
17. J. B. Pendry, A. J. Holden, D. J. Robbins, and W. J. Stewart, "Magnetism from conductors and enhanced nonlinear phenomena," *IEEE T. Microw. Theory* **47**(11), 2075–2084 (1999).
18. C. Enkrich, M. Wegener, S. Linden, S. Burger, L. Zschiedrich, F. Schmidt, J. F. Zhou, T. Koschny, and C. M. Soukoulis, "Magnetic metamaterials at telecommunication and visible frequencies," *Phys. Rev. Lett.* **95**(20), 203901 (2005).
19. N. Katsarakis, G. Konstantinidis, A. Kostopoulos, R. S. Penciu, T. F. Gundogdu, M. Kafesaki, E. N. Economou, T. Koschny, and C. M. Soukoulis, "Magnetic response of split-ring resonators in the far-infrared frequency regime," *Opt. Lett.* **30**(11), 1348–1350 (2005).
20. V. Delgado, O. Sydoruk, E. Tatartschuk, R. Marqués, M. J. Freire, and L. Jelinek, "Analytical circuit model for split ring resonators in the far infrared and optical frequency range," *Metamaterials (Amst.)* **3**(2), 57–62 (2009).
21. X. Shi, R. L. Thornton, and L. Hesselink, "Nano-aperture with 1000x power throughput enhancement for very small aperture laser system (VSAL)," in *Optical Data Storage 2001* (SPIE, 2002), **4342**, pp. 320–327.
22. K. Şendur, C. Peng, and W. Challener, "Near-field radiation from a ridge waveguide transducer in the vicinity of a solid immersion lens," *Phys. Rev. Lett.* **94**(4), 043901 (2005).
23. J. B. Leen, P. Hansen, Y. T. Cheng, A. Gibby, and L. Hesselink, "Near-field optical data storage using C-apertures," *Appl. Phys. Lett.* **97**(7), 073111 (2010).
24. N. Zhou, E. C. Kinzel, and X. Xu, "Nanoscale ridge aperture as near-field transducer for heat-assisted magnetic recording," *Appl. Opt.* **50**(31), G42–G46 (2011).
25. S. Tretyakov, "On geometrical scaling of split-ring and double-bar resonators at optical frequencies," *Metamaterials (Amst.)* **1**(1), 40–43 (2007).
26. T. D. Corrigan, P. W. Kolb, A. B. Sushkov, H. D. Drew, D. C. Schmadel, and R. J. Phaneuf, "Optical plasmonic resonances in split-ring resonator structures: an improved LC model," *Opt. Express* **16**(24), 19850–19864 (2008).
27. C. Rockstuhl, T. Zentgraf, H. Guo, N. Liu, C. Etrich, I. Loa, K. Syassen, J. Kuhl, F. Lederer, and H. Giessen, "Resonances of split-ring resonator metamaterials in the near infrared," *Appl. Phys. B-Lasers O.* **84**(1–2), 219–227 (2006).
28. A. W. Clark, A. K. Sheridan, A. Glidle, D. R. S. Cumming, and J. M. Cooper, "Tunable visible resonances in crescent shaped nano-split-ring resonators," *Appl. Phys. Lett.* **91**(9), 093109 (2007).
29. P. Ding, E. J. Liang, W. Q. Hu, G. W. Cai, and Q. Z. Xue, "Tunable plasmonic properties and giant field enhancement in asymmetric double split ring arrays," *Photon. Nanostructures* **9**(1), 42–48 (2011).
30. H. O. Moser, B. D. F. Casse, O. Wilhelmi, and B. T. Saw, "Terahertz response of a microfabricated rod-split-ring-resonator electromagnetic metamaterial," *Phys. Rev. Lett.* **94**(6), 063901 (2005).
31. D. R. Smith, W. J. Padilla, D. C. Vier, S. C. Nemat-Nasser, and S. Schultz, "Composite medium with simultaneously negative permeability and permittivity," *Phys. Rev. Lett.* **84**(18), 4184–4187 (2000).
32. N. Katsarakis, T. Koschny, M. Kafesaki, E. N. Economou, and C. M. Soukoulis, "Electric coupling to the magnetic resonance of split ring resonators," *Appl. Phys. Lett.* **84**(15), 2943–2945 (2004).
33. A. Datta and X. Xu, "Infrared Near-Field Transducer for Heat-Assisted Magnetic Recording," *IEEE Trans. Magn.* **53**(12), 1–5 (2017).
34. Z. H. Cen, B. X. Xu, J. F. Hu, J. M. Li, K. M. Cher, Y. T. Toh, K. D. Ye, and J. Zhang, "Optical property study of FePt-C nanocomposite thin film for heat-assisted magnetic recording," *Opt. Express* **21**(8), 9906–9914 (2013).
35. P. B. Johnson and R.-W. Christy, "Optical constants of the noble metals," *Phys. Rev. B* **6**(12), 4370–4379 (1972).
36. A. Datta and X. Xu, "Improved Near-Field Transducer Design for Heat-Assisted Magnetic Recording," *IEEE Trans. Magn.* **52**(12), 1–6 (2016).
37. N. Berkovitch, P. Ginzburg, and M. Orenstein, "Nano-plasmonic antennas in the near infrared regime," *J. Phys. Condens. Matter* **24**(7), 073202 (2012).
38. N. Zhou, Y. Li, and X. Xu, "Resolving near-field from high order signals of scattering near-field scanning optical microscopy," *Opt. Express* **22**(15), 18715–18723 (2014).

39. B. Knoll and F. Keilmann, "Enhanced dielectric contrast in scattering-type scanning near-field optical microscopy," *Opt. Commun.* **182**(4–6), 321–328 (2000).